

Polyhedral Voronoi diagrams for additive manufacturing, Supplemental material

JONÀS MARTÍNEZ, SAMUEL HORNUS, HAICHUAN SONG, and SYLVAIN LEFEBVRE, Université de Lorraine, CNRS, Inria, LORIA, F-54000 Nancy, France

CCS Concepts: • Computing methodologies → Shape modeling;

Additional Key Words and Phrases: Voronoi diagram, 3D printing, additive manufacturing

ACM Reference Format:

Jonàs Martínez, Samuel Hornus, Haichuan Song, and Sylvain Lefebvre. 2018. Polyhedral Voronoi diagrams for additive manufacturing, Supplemental material. *ACM Trans. Graph.* 37, 4, Article 129 (August 2018), 7 pages. <https://doi.org/10.1145/3197517.3201343>

Polyhedral Voronoi diagrams and algorithm

In Section 1 we provide the rationale behind the construction of Polyhedral bisectors (Section 1.1), how to find the normal of bisector facets (Section 1.2), and how to identify any bisector local minima that may violate fabrication constraints (Section 1.3).

In Section 2, we detail a 3-parameters family of cone distances that satisfy the fabrication constraints but that we have not experimented with yet.

In Section 3 we prove that the polyhedral distance respects the triangular inequality.

In Section 4, we explain how we compute the labels in the labels grid. The details are important for obtaining a reasonably efficient implementation.

Elastic behavior

In Section 5, we give the analytic expressions for the orthotropic compliance tensor and the bulk modulus bounds.

Sections 6 and 7 provide the elasticity tensors for Figures 16 and 17 in the article.

In Figure 3 and Figure 4 we provide the Poisson's ratio and shear modulus, respectively, of Figure 12 in the article.

1 CONSTRUCTIONS

We say that two features $X \subset P$ and $Y \subset P$ on the boundary of the distance polytope P generate a feature B of the bisector $\mathcal{B}(p, q)$ when

$$B = \{(p + \lambda X) \cap (q + \lambda Y) \mid \lambda > 0\}. \quad (1)$$

B is empty or not depending on the relative position of the point sites p and q .

Permission to make digital or hard copies of all or part of this work for personal or classroom use is granted without fee provided that copies are not made or distributed for profit or commercial advantage and that copies bear this notice and the full citation on the first page. Copyrights for components of this work owned by others than the author(s) must be honored. Abstracting with credit is permitted. To copy otherwise, or republish, to post on servers or to redistribute to lists, requires prior specific permission and/or a fee. Request permissions from permissions@acm.org.

© 2018 Copyright held by the owner/author(s). Publication rights licensed to ACM. 0730-0301/2018/8-ART129 \$15.00 <https://doi.org/10.1145/3197517.3201343>

1.1 Construction of a bisector

Given two point sites p and q , let us define the unit vector $u = \frac{q-p}{\|q-p\|}$. The facets of P can be partitioned into front and back facets, where the normal vector of a front (resp. back) facet has a non-negative (resp. non-positive) dot-product with u . A point r on the bisector $\mathcal{B}(p, q)$ can be written as $r = p + \lambda r_i = q + \lambda r_j$ where $\lambda = dp(p, r) = dp(q, r)$, r_i is a point of a front-facet of P , r_j is a point of a back-facet of P and the line $(r_i r_j)$ is also parallel to the vector u . Conversely, given a point r_i on a front-facet and a point r_j on a back-facet; if both points also lie on a line parallel to u , then they generate (in the sense given above) exactly one point on the bisector. This proves that the bisector $\mathcal{B}(p, q)$ can be constructed from the overlay O of the projections of the front facets and the back facets on a plane orthogonal to vector u , through a function $\phi : O \mapsto \mathcal{B}(p, q)$: Let v be a vertex of a cell of the overlay. The points $r_i(v)$ and $r_j(v)$ are computed as the intersection of P with the line through v parallel to the vector u . These two points on P generate the bisector point $\phi(v) = p + \lambda(v)r_i(v) = q + \lambda(v)r_j(v)$ where $\lambda(v) = \frac{\|q-p\|}{\|r_i(v) - r_j(v)\|}$. Once the vertices of the bisector are computed, its facets are trivially obtained since they follow the same combinatorics as the overlay. Finally, silhouette vertices on the boundary of the overlay are mapped to bisector points at infinity.

The present submission comes with a compiled javascript interactive visualization of the polyhedral bisector. The reader is invited to check the “bisector/” directory and the “README.txt” file in the parent directory.

1.2 Normal vector of a bisector facet

Let f be a facet of the bisector $\mathcal{B}(p, q)$ generated by the facets f_i and f_j of P . (In particular, the projections of both facets on a plane orthogonal to $q - p$ have a non-empty intersection, which is a cell of the overlay mentioned in Section 1.1.) Let n_i be the outward normal vector to facet f_i . Let $\alpha_i > 0$ be the distance from the origin to the plane H_i supporting f_i . In particular, if r_i is a point of f_i then $\alpha_i = r_i \cdot n_i$.

PROPOSITION 1.1 ([Icking and Ha 2001]). *Write H_{ij} for the plane that spans the origin and the line $H_i \cap H_j$. The bisector facet f (generated by f_i and f_j) is parallel to the plane H_{ij} and its normal vector is proportional to $\alpha_j n_i - \alpha_i n_j$.*

PROOF. We prove the formula for the normal vector. Let $r_i \in f_i$ and $r_j \in f_j$ be the pair of features that generates a point $\phi(v)$ where

v is any point on the line $(r_i r_j)$. We have

$$\phi(v) \cdot (\alpha_j n_i) = (p + \lambda(v)r_i) \cdot (\alpha_j n_i) \quad (2)$$

$$= K + \lambda(v)\alpha_j(r_i \cdot n_i) = K + \lambda(v)\alpha_j\alpha_i \quad (3)$$

$$\text{and } \phi(v) \cdot (\alpha_i n_j) = (q + \lambda(v)r_j) \cdot (\alpha_i n_j) \quad (4)$$

$$= K' + \lambda(v)\alpha_i(r_j \cdot n_j) = K' + \lambda(v)\alpha_i\alpha_j, \quad (5)$$

$$\text{with } K = \alpha_j n_i \cdot p \quad (6)$$

$$\text{and } K' = \alpha_i n_j \cdot q. \quad (7)$$

We see that $\phi(v) \cdot (\alpha_j n_i - \alpha_i n_j)$ is a constant for any point v in the given overlay cell. \square

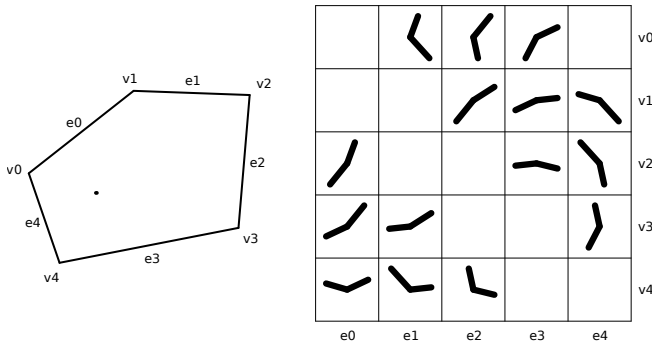


Fig. 1. The 15 possible bisector vertex configurations induced by a 5 sided polygon P , corresponding to all the possible interactions between edges (horizontal axis) and vertices (vertical axis) of P . Vertex v_4 generates two local-minimum configurations with edges e_0 and e_1 . Therefore the particular polyhedral distance induced by this polygon does not produce fabricable Voronoi diagrams.

1.3 Finding a local minimum

Let e be a directed line segment on P (for example, an edge, but not necessarily; we see e also as a vector). Let f_i a facet of P not parallel to e , with outward normal vector n_i . Then for some directions $p - q$, segment e and facet f_i do generate a line segment e' on the bisector $\mathcal{B}(p, q)$. Let l and l' be the lines supporting segments e and e' respectively. Then l' is parallel to the line from the origin to the point $x = l \cap H_i$. As a point walks along e , the corresponding bisector point walks along e' in the direction x if $e \wedge n_i > 0$, and in the opposite direction, $-x$, otherwise.

A vertex v of the bisector $\mathcal{B}(p, q)$ is the image through ϕ of a vertex of the overlay O . Thus, vertex v is generated either by a vertex v_i and a facet f_j of P (that can not contain v_i) or by two edges e_i and e_j of P . In either case, the argument above lets us compute the directions (in \mathbb{R}^3) of each bisector edge emanating from v . If the z -component of every direction is positive, then v is a local minimum. This gives an algorithm to decide in quadratic time whether or not a distance polytope can produce local minimum in the derived polyhedral Voronoi diagram. Figure 1 shows all the bisector vertex configurations for a 2D polygonal distance.

2 VARYING σ , ζ , μ AND θ

If we increase θ , then ℓ decreases and the apex moves down. We can take it back up to its original position by also increasing μ . We then obtain a 3-parameters family of cones whose parameters can spatially vary together and independently while respecting both fabrication constraints. Parameters θ (represented by $\ell = \tan(\pi/2 - \theta)$) and μ are related by

$$\ell^2 = \frac{A_z^2}{\mu^2} - (1 + A_z)^2. \quad (8)$$

Changes in the Voronoi mesh. When increasing θ , the bisector facets generated by a side facet and the base facet of the distance cone become more vertical. Then, to compensate the lowering of the apex, we also increase μ according to Equation (8). We also expect this compensation to raise the slope of the bisector facets (Main paper, Section 4.3.3). Therefore, we can interpret the μ - θ pair as working in tandem for us to tune the stiffness in z . In the horizontal plane, we can still choose σ and ζ at will to control horizontal stiffness.

3 TRIANGULAR INEQUALITY

Let P be a convex compact set that contains the origin in its interior so that the induced distance d_P is well defined.

PROPOSITION 3.1. *Let λ and μ be two positive real numbers. $\lambda > 0, \mu > 0$. Then $(\lambda + \mu)P = \lambda P + \mu P$.*

PROOF. Let p be a point in $(\lambda + \mu)P$. There exists a point $x \in P$ such that $p = (\lambda + \mu)x = \lambda x + \mu x$. So $p \in (\lambda P + \mu P)$ and $(\lambda + \mu)P \subset \lambda P + \mu P$.

Let p be a point in $\lambda P + \mu P$. There exist two points x and y in P such that $p = \lambda x + \mu y$. We can write $p = (\lambda + \mu)q$ where $q = \frac{\lambda}{\lambda + \mu}x + \frac{\mu}{\lambda + \mu}y$. Since P is convex, the point q is in P . Therefore, $p \in (\lambda + \mu)P$ and $\lambda P + \mu P \subset (\lambda + \mu)P$. \square

PROPOSITION 3.2. *The induced distance d_P satisfies the triangular inequality.*

PROOF. Let p, q and r be three points. Let $\lambda = d_P(p, q)$ and $\mu = d_P(q, r)$. By definition, $q \in (p + \lambda P)$ and $r \in (q + \mu P)$. This implies that $r \in (p + \lambda P + \mu P)$. By Proposition 3.1, $r \in (p + (\lambda + \mu)P)$. By definition of d_P , we have $d_P(p, r) \leq \lambda + \mu = d_P(p, q) + d_P(q, r)$. \square

4 ALGORITHMIC DETAILS

Let $C \subset \mathbb{R}^3$ be the input solid to be filled with our microstructure mesh \mathcal{K} . In a slice at height d , the deposition paths that form the microstructure are given by $B_d \cap \mathcal{K} \cap C$. Since \mathcal{K} is piecewise linear, $B_d \cap \mathcal{K}$ is composed of a set of line segments.

A sweep-plane approach to compute $B_d \cap \mathcal{K}$ would be ideally suited for our setting since we do want to extract many horizontal slices of \mathcal{K} . Such an algorithm involves updating the planar topology of $B_d \cap \mathcal{K}$ as d varies monotonously. Dehne *et al.* [1997] studied the two dimensional setting of the wavefront approach for convex metrics. In the same vein, Chen *et al.* [2006] presented a sweep-line algorithm for certain polygonal metrics in the plane. However, to the best of our knowledge there exists no work dealing with the

three-dimensional case. This is mostly due to the complicated update of the sweep-plane, and the difficulties in obtaining a robust implementation [Chen et al. 2006].

Instead, we propose a simpler discretized approach to approximate the deposition paths, that we illustrate in Figure 11. We overlay a 2D regular grid over $C \cap B_d$, called the *labels grid* and label each grid square with the site of S closest to the square center, as measured by the polyhedral distance d_P . Then, we extract all the boundary edges between adjacent grid squares with different labels and simplify the extracted jagged paths in order to produce the final deposition paths for fabricating the microstructure inside C .

The *labels grid* should not be confused with the 3D *sites grid*, defined in Section 4.3.1: the labels grid is 2D and much denser.

4.1 Voronoi labeling

This section describes the labeling of each square of the 2D labels grid. The size of each such square should be much smaller than the size of the finest cells of the sites grid. In our experiments, it is set from $20\text{ }\mu\text{m}$ to $100\text{ }\mu\text{m}$. The labels grid samples the horizontal plane B_d at height $z = d$. For a given grid square center point c , we need to compute the point site $v(c) \in S$ closest to c , that will serve as a label for that square. (Note that the query point c is located in \mathbb{R}^3 and $c_z = d$.) Let s_c be the cell of the sites grid that contains the query c . To find $v(c)$ efficiently, we traverse a pre-computed list of cells around s_c : $v(c) = \operatorname{argmin}_{s \in s_p + \Sigma} d_P(s, c)$. The list Σ stores 3D indices *relative* to the reference cell C_0 with index $(0, 0, 0)$ and is sorted by distance to C_0 . The computation of Σ is detailed below.

4.2 Computation of Σ with a uniform distance

The idea is to obtain an upper bound λ_{\max} on the distance between the query point c and its nearest site $v(c)$ and then store in Σ the indices of all the cells that are at distance no greater than λ_{\max} from the reference cell C_0 .

Recall that the distance d_P is not symmetric. Since we want to center the search around the query point c , we make the following observation. Writing P' for the reflection of P with respect to the origin, we have $d_P(s, c) = d_{P'}(c, s)$ and $\forall \lambda \geq 0, d_P(s, c) \leq \lambda \iff c \in s + \lambda P \iff s \in c + \lambda P'$. We are then guaranteed that $v(c)$ lies inside $c + \lambda_{\max} P'$, which lets us restrict the search.

To compute the upper bound λ_{\max} for our specific point site distribution (Section 4.3.1), we use the following property: If we can fit an axis-aligned cube of side length $2a$ into the scaled unit-ball λP for some $\lambda > 0$ (Figure 2-left), then we have the guarantee that *any* translate of λP (or of $\lambda P'$, in particular, $c + \lambda P'$) contains at least one cell of a regular grid whose cells have side length a (Figure 2-middle). If s is a point site in that cell, then $s \in c + \lambda P' \iff d_P(s, c) \leq \lambda$. From the particular geometry of the unit-ball that we use (a polyhedral cone, Section 4.2), we can (conservatively) fit a cube touching the base of the cone and of side length $L = \frac{(1+A_z)\sqrt{2}\ell}{1+A_z+\sqrt{2}\ell}$ where $1+A_z$ is the height of the cone and $\ell/\cos(\pi/k)$ is the radius of its base for some integer $k \geq 3$. Thus, if the sites grid cells have side-length a , the nearest site of any query point is at polyhedral-distance no more than $\lambda_{\max} = \frac{2a}{L}$ from the query. (In our implementation, we scale the problem so that $a = 1$.)

Using a breadth-first traversal starting at C_0 , we pre-compute the search list Σ of cell indices (in the sites grid) The search-list is truncated when the distance reaches λ_{\max} .

Remark. Our “jittered grid” site distribution scheme gives us an easy-to-compute upper bound on the distance from any query point in \mathbb{R}^3 to the nearest point site in S . Nonetheless, such an upper bound can also be derived for other point sampling schemes and used in our technique.

Computing distances. The distance $d_{P'}$ between a point and an axis-aligned cubical cell is computed efficiently using a simple modification of Greene’s technique [1994]. During the computation of the search-list, one needs to compute the polyhedral distance between two grid cells:

$$d_{P'}(C_0, C) = \min\{\lambda : \exists a \in C_0, \exists b \in C, b \in a + \lambda P'\} \quad (9)$$

$$= \min\{\lambda : \exists p \in (C \ominus C_0), p \in \lambda P'\} \quad (10)$$

$$= d_{P'}(O, C \ominus C_0). \quad (11)$$

where O is the origin and $C \ominus C_0 = \{b - a : a \in C_0, b \in C\}$ is a cube twice the size of C or C_0 . Since we stop the construction of the search list Σ when the distance gets larger than λ_{\max} , the list Σ contains precisely the indices of the sites grid cells that touch the Minkowski sum of C_0 and $\lambda_{\max} P'$ (Figure 2-right).

In a multi-resolution sites grid, we use the precomputed search-list only at the coarsest level of the sites grid. Then, when a cell should be recursively subdivided, we check that each sub-cell is at distance no more than the current minimal distance $\lambda \leq \lambda_{\max}$ found so far before examining the site(s) that it contains. Greene’s technique is easily modified to exit as soon as the cell is found to be farther from the query point than λ .

4.3 Computation of Σ with a spatially varying distance

When the parameters of the cone distance vary spatially, the distances to the sites grid cells must be conservatively under-approximated in order to account for the variation of the distances used at each different sites.

Both for computing the search list Σ and during the search of the nearest site for a given query point, we use a separate, larger distance cone P^{big} which is guaranteed to contain all the distance cones defined at the point sites $\{P(s) : s \in S\}$. Instead of computing λ_{\max} on this cone, we use the largest λ_{\max} among the values computed for all the possible distance cones: $\lambda_{\max}^{\text{big}} = \max_{s \in S} \lambda_{\max}(P(s))$. The search is then slower, but is sure to find the correct nearest site.

5 ELASTIC BEHAVIOR AND HOMOGENIZATION

For linear elasticity we have that $\sigma = C\epsilon$ and conversely $\epsilon = S\sigma$, where σ is the stress, ϵ is the strain, C is the elasticity tensor, and S is the compliance tensor.

We follow the conventional homogenization method [Andreassen and Andreassen 2014] of prescribing the strain and computing the overall stress response for the six unit strains in order to approximate the elasticity tensor C . We obtain the compliance tensor S by directly inverting C .

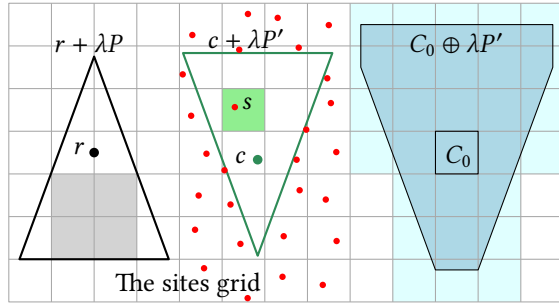


Fig. 2. *Left.* One translate of the scaled polytope λP contains a 2×2 sub-grid. *Middle.* This guarantees that any translate of $\lambda P'$ contains at least one grid cell (green), thus at least one point site (red). *Right.* The blue cells have their index in the search list Σ .

5.1 Orthotropic materials

The compliance tensor S_{ortho} of an ideal orthotropic material [Jones 1975] is:

$$S_{\text{ortho}} = \begin{pmatrix} s_{11} & s_{12} & s_{13} & 0 & 0 & 0 \\ s_{12} & s_{22} & s_{23} & 0 & 0 & 0 \\ s_{13} & s_{23} & s_{33} & 0 & 0 & 0 \\ 0 & 0 & 0 & s_{44} & 0 & 0 \\ 0 & 0 & 0 & 0 & s_{55} & 0 \\ 0 & 0 & 0 & 0 & 0 & s_{66} \end{pmatrix} \quad (12)$$

where,

$$s_{11} = \frac{1}{E_x}, \quad s_{22} = \frac{1}{E_y}, \quad s_{33} = \frac{1}{E_z} \quad (13)$$

$$s_{44} = \frac{1}{G_{yz}}, \quad s_{55} = \frac{1}{G_{zx}}, \quad s_{66} = \frac{1}{G_{xy}} \quad (14)$$

$$s_{12} = -\frac{v_{yx}}{E_y} = -\frac{v_{xy}}{E_x}, \quad s_{13} = -\frac{v_{zx}}{E_z} = -\frac{v_{xz}}{E_x}, \quad (15)$$

$$s_{23} = -\frac{v_{zy}}{E_z} = -\frac{v_{yz}}{E_y} \quad (16)$$

such that

$$\frac{v_{ij}}{E_i} = \frac{v_{ji}}{E_j} \quad i, j = x, y, z \quad i \neq j \quad (17)$$

and E_i is the Young's modulus along axis i (measure of stiffness), G_{ij} is the shear modulus in direction j on the plane whose normal is in direction i (measure of response to shear stress), and v_{ij} is the Poisson's ratio (ratio of transverse strain to axial strain) that corresponds to a contraction in direction j when an extension is applied in direction i .

Given a homogenized compliance tensor S , we compute the closest orthotropic compliance tensor S_{ortho} under the logarithmic Euclidean distance [Moakher and Norris 2006], which is well-suited for elasticity.

5.2 Bulk modulus

We are also interested in evaluating the overall compressive strength. To do so, we consider the bulk modulus K , that characterizes the tendency of a material to deform in all directions when uniformly loaded in all directions. A high bulk modulus implies higher material incompressibility. Given the following classical bulk modulus bounds [Hill 1952]

$$K_V = ((c_{11} + c_{22} + c_{33}) + 2(c_{12} + c_{23} + c_{31}))/9 \quad (\text{Voigt average})$$

$$K_R = ((s_{11} + s_{22} + s_{33}) + 2(s_{12} + s_{23} + s_{31}))^{-1} \quad (\text{Reuss average}) \quad (18)$$

we consider the Voigt-Reuss average $K_{VR} = (K_V + K_R)/2$.

6 HOMOGENIZED ELASTICITY TENSORS FIGURE 16 IN ARTICLE

Tensors values are rounded to three decimals. Interestingly, the elasticity tensor of (Figure 16b) is well approximated by a monoclinic material (single plane of tensor symmetry, 13 independent constants), while the others are better approximated by an orthotropic one (three planes of tensor symmetry, 9 independent constants). For more details about tensor symmetries and elastic constants see for instance Section 2.2 in [Jones 1975].

6.1 Polyhedral Voronoi diagram (Figure 16a)

$$C = \begin{pmatrix} 0.197 & 0.077 & 0.07 & 0.0 & 0.0 & 0.0 \\ 0.077 & 0.195 & 0.069 & 0.0 & 0.0 & 0.0 \\ 0.07 & 0.069 & 0.253 & 0.0 & 0.0 & 0.0 \\ 0.0 & 0.0 & 0.0 & 0.06 & 0.0 & 0.0 \\ 0.0 & 0.0 & 0.0 & 0.0 & 0.077 & 0.0 \\ 0.0 & 0.0 & 0.0 & 0.0 & 0.0 & 0.076 \end{pmatrix}$$

6.2 Tessellation three planes (Figure 16b)

$$C = \begin{pmatrix} 0.127 & 0.098 & 0.083 & 0.0 & -0.035 & 0.0 \\ 0.096 & 0.227 & 0.077 & 0.0 & -0.018 & 0.0 \\ 0.081 & 0.077 & 0.313 & 0.0 & -0.029 & 0.0 \\ 0.0 & 0.0 & 0.0 & 0.094 & 0.0 & -0.021 \\ -0.034 & -0.02 & -0.032 & 0.0 & 0.088 & 0.0 \\ 0.0 & 0.0 & 0.0 & -0.021 & 0.0 & 0.08 \end{pmatrix}$$

6.3 Polyhedral Voronoi diagram (Figure 16c)

$$C = \begin{pmatrix} 0.118 & 0.083 & 0.083 & 0.0 & 0.0 & 0.0 \\ 0.084 & 0.259 & 0.072 & 0.0 & 0.0 & 0.0 \\ 0.084 & 0.072 & 0.259 & 0.0 & 0.0 & 0.0 \\ 0.0 & 0.0 & 0.0 & 0.084 & 0.0 & 0.0 \\ 0.0 & 0.0 & 0.0 & 0.0 & 0.084 & 0.0 \\ 0.0 & 0.0 & 0.0 & 0.0 & 0.0 & 0.075 \end{pmatrix}$$

6.4 Tessellation four planes (Figure 16d)

$$C = \begin{pmatrix} 0.201 & 0.075 & 0.067 & 0.0 & 0.0 & 0.0 \\ 0.075 & 0.202 & 0.068 & 0.0 & 0.0 & 0.0 \\ 0.067 & 0.068 & 0.207 & 0.0 & 0.0 & 0.0 \\ 0.0 & 0.0 & 0.0 & 0.064 & 0.0 & 0.0 \\ 0.0 & 0.0 & 0.0 & 0.0 & 0.074 & 0.0 \\ 0.0 & 0.0 & 0.0 & 0.0 & 0.0 & 0.074 \end{pmatrix}$$

6.5 Polyhedral Voronoi diagram (Figure 16e)

$$C = \begin{pmatrix} 0.002 & 0.003 & 0.003 & 0.0 & 0.0 & 0.0 \\ 0.004 & 0.28 & 0.071 & 0.0 & 0.0 & 0.0 \\ 0.003 & 0.07 & 0.264 & 0.0 & 0.0 & 0.0 \\ 0.0 & 0.0 & 0.0 & 0.002 & 0.0 & 0.0 \\ 0.0 & 0.0 & 0.0 & 0.0 & 0.002 & 0.0 \\ 0.0 & 0.0 & 0.0 & 0.0 & 0.0 & 0.1 \end{pmatrix}$$

7 HOMOGENIZED ELASTICITY TENSORS FIGURE 17 IN ARTICLE

7.1 Left compression test ($\mu = 0.6, \sigma = 1$)

$$C = \begin{pmatrix} 0.06 & 0.024 & 0.019 & 0.0 & 0.0 & 0.0 \\ 0.024 & 0.061 & 0.019 & 0.0 & 0.0 & 0.0 \\ 0.018 & 0.019 & 0.058 & 0.0 & 0.0 & 0.0 \\ 0.0 & 0.0 & 0.0 & 0.017 & 0.0 & 0.0 \\ 0.0 & 0.0 & 0.0 & 0.0 & 0.026 & 0.0 \\ 0.0 & 0.0 & 0.0 & 0.0 & 0.0 & 0.026 \end{pmatrix}$$

7.2 Middle compression test ($\mu = 0.6, \sigma = 0.4$)

$$C = \begin{pmatrix} 0.012 & 0.016 & 0.012 & 0.0 & 0.0 & 0.0 \\ 0.018 & 0.16 & 0.042 & 0.0 & 0.0 & 0.0 \\ 0.013 & 0.042 & 0.145 & 0.0 & 0.0 & 0.0 \\ 0.0 & 0.0 & 0.0 & 0.012 & 0.0 & 0.0 \\ 0.0 & 0.0 & 0.0 & 0.0 & 0.017 & 0.0 \\ 0.0 & 0.0 & 0.0 & 0.0 & 0.0 & 0.059 \end{pmatrix}$$

7.3 Right compression test ($\mu = 0.85, \sigma = 1$)

$$C = \begin{pmatrix} 0.06 & 0.03 & 0.023 & 0.0 & 0.0 & 0.0 \\ 0.031 & 0.06 & 0.024 & 0.0 & 0.0 & 0.0 \\ 0.025 & 0.025 & 0.148 & 0.0 & 0.0 & 0.0 \\ 0.0 & 0.0 & 0.0 & 0.013 & 0.0 & 0.0 \\ 0.0 & 0.0 & 0.0 & 0.0 & 0.035 & 0.0 \\ 0.0 & 0.0 & 0.0 & 0.0 & 0.0 & 0.035 \end{pmatrix}$$

REFERENCES

- Erik Andreassen and Casper Schousboe Andreassen. 2014. How to Determine Composite Material Properties Using Numerical Homogenization. *Computational Materials Science* 83 (2014), 488–495. <https://doi.org/10.1016/j.commatsci.2013.09.006>
- Zhenming Chen, Evanthia Papadopoulou, and Jinhui Xu. 2006. Robustness of k-gon Voronoi diagram construction. *Inform. Process. Lett.* 97, 4 (2006), 138–145. <https://doi.org/10.1016/j.ipl.2005.10.009>
- F. Dehne and R. Klein. 1997. “The big sweep”: On the power of the wavefront approach to Voronoi diagrams. *Algorithmica* 17, 1 (1997), 19–32. <https://doi.org/10.1007/BF02523236>
- Ned Greene. 1994. Detecting Intersection of a Rectangular Solid and a Convex Polyhedron. In *Graphics Gems IV*, Paul S. Heckbert (Ed.). Academic Press, Chapter 1.7, 74–82.
- Richard Hill. 1952. The elastic behaviour of a crystalline aggregate. *Proceedings of the Physical Society. Section A* 65, 5 (1952), 349.
- Christian Icking and Lihong Ha. 2001. A Tight Bound for the Complexity of Voronoi Diagrams Under Polyhedral Convex Distance Functions in 3D. In *Proceedings of the Thirty-third Annual ACM Symposium on Theory of Computing*. 316–321. <https://doi.org/10.1145/380752.380815>
- Robert M Jones. 1975. *Mechanics of Composite Materials*. Vol. 193. Scripta Book Company Washington, DC.
- Maher Moakher and Andrew N. Norris. 2006. The Closest Elastic Tensor of Arbitrary Symmetry to an Elasticity Tensor of Lower Symmetry. *Journal of Elasticity* 85, 3 (2006), 215–263. <https://doi.org/10.1007/s10659-006-9082-0>

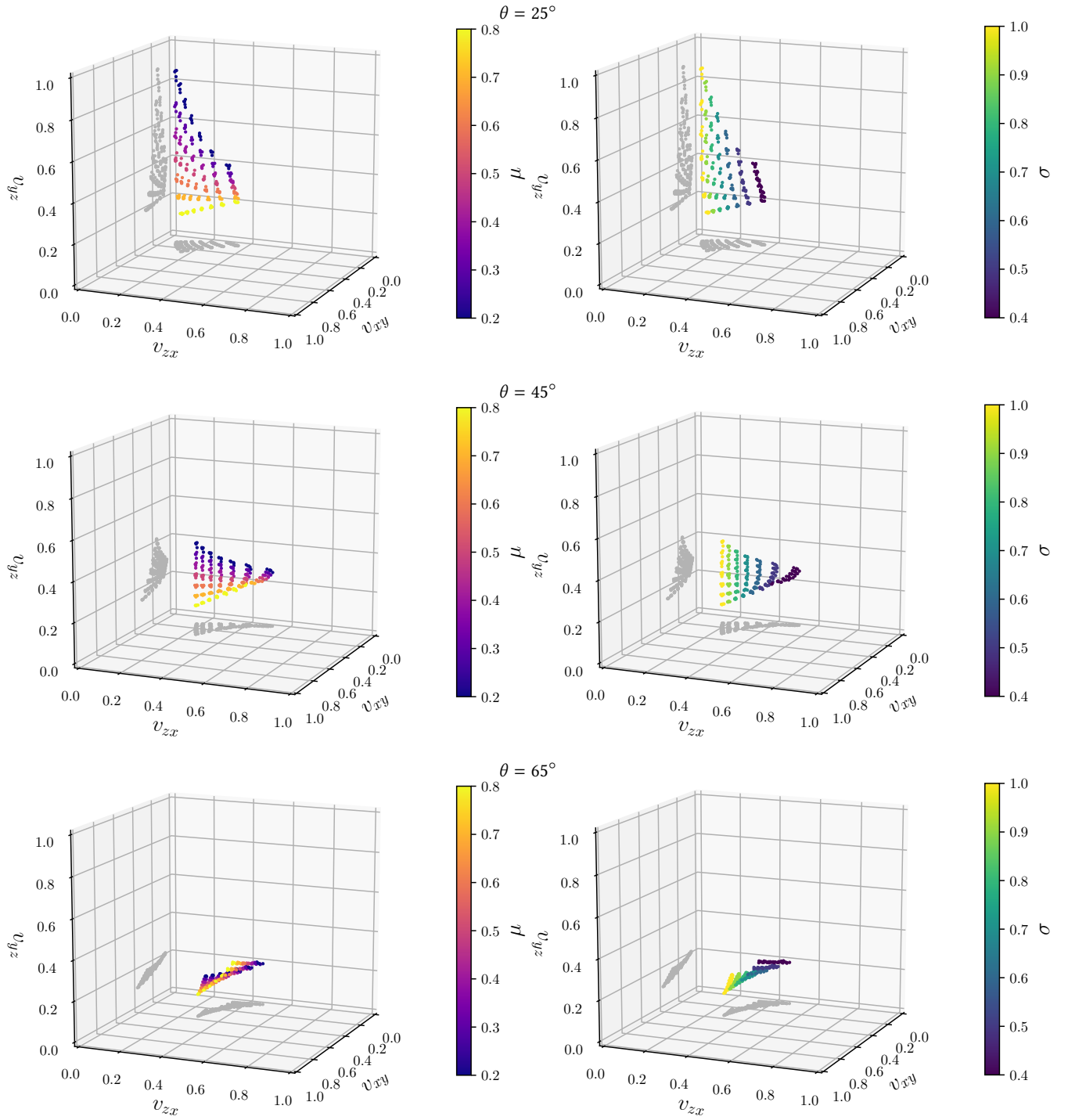


Fig. 3. Material space for $k = 8$. Each row corresponds to a different minimal bisector slope θ . Each plot dot denotes a single test. The plot axes correspond to the three orthogonal Poisson's ratio. The color of dots either depicts μ (left column) or σ (right column).

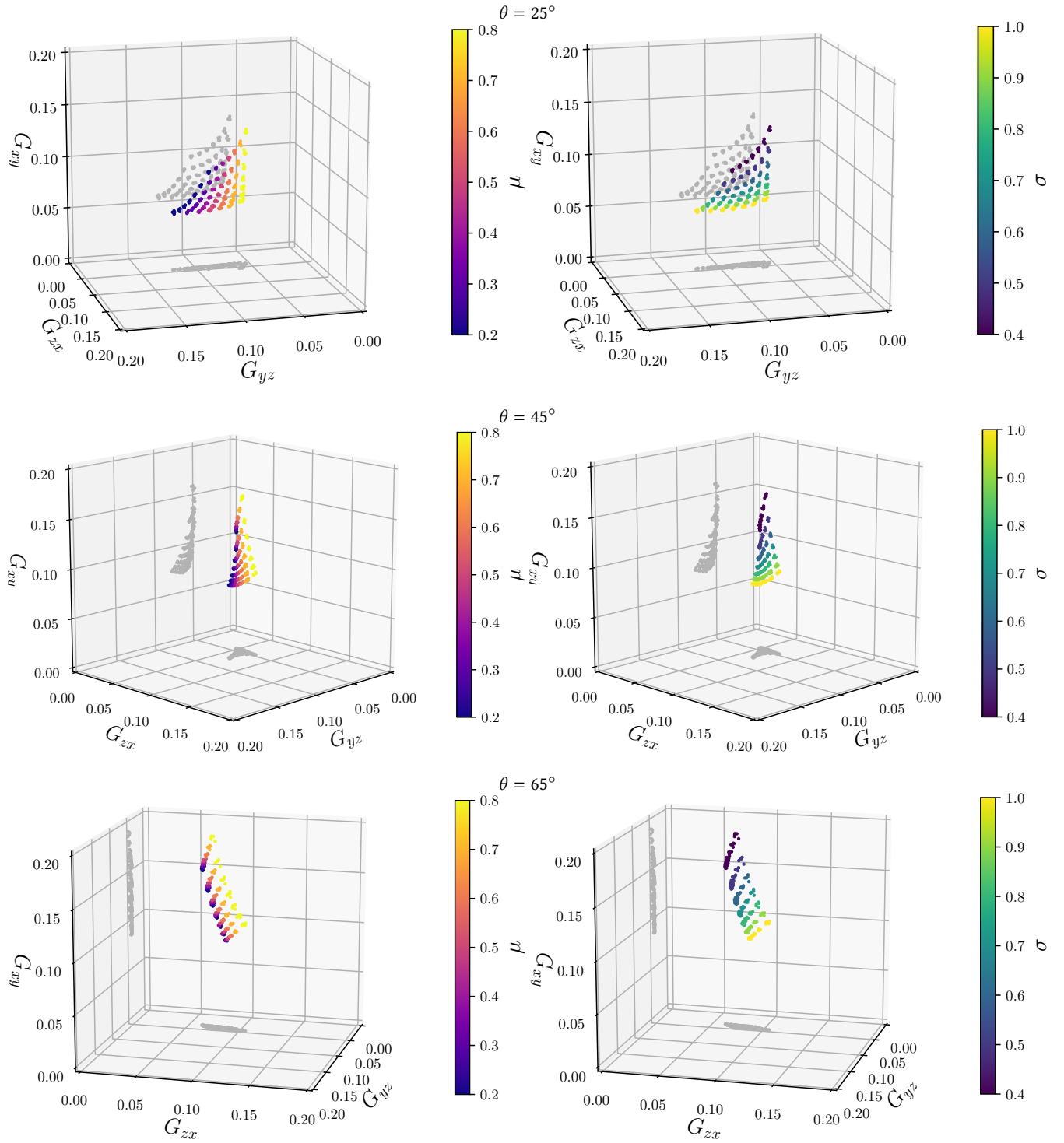


Fig. 4. Material space for $k = 8$. Each row corresponds to a different minimal bisector slope θ . Each plot dot denotes a single test. The plot axes correspond to the three orthogonal shear moduli. The color of dots either depicts μ (left column) or σ (right column).